

Dynamic Laser Absorptance Measured in a Geometrically Characterized Stainless-Steel Powder Layer


Brian J. Simonds^{1,*}, Edward J. Garboczi², Todd A. Palmer^{3,4}, and Paul A. Williams¹

¹*Physical Measurement Laboratory, National Institute of Standards and Technology, Boulder, Colorado 80305, USA*

²*Materials Measurement Laboratory, National Institute of Standards and Technology, Boulder, Colorado 80305, USA*

³*Department of Engineering Science and Mechanics, Pennsylvania State University, University Park, Pennsylvania 16802, USA*

⁴*Department of Materials Science and Engineering, Pennsylvania State University, University Park, Pennsylvania 16802, USA*

 (Received 11 September 2019; revised manuscript received 6 November 2019; accepted 23 December 2019; published 21 February 2020)

The relationship between real powder distributions and optical coupling is a critical building block for developing a deeper physical understanding of laser-additive manufacturing and for creating more reliable and accurate models for predictable manufacturing. Laser-light absorption by a metal powder is distinctly different from that of a solid material, as it is impacted by additional parameters, such as particle size, shape distribution, and packing. Here, we use x-ray computed tomography to experimentally determine these parameters in a thinly spread austenitic stainless-steel powder on a metal substrate, and we combine these results with optical absorptance measurements during a 1 ms stationary laser-light exposure to simulate the additive-manufacturing process. Within the thinly spread powder layer, the particle volume fraction changes continuously from near zero at the powder surface to a peak value of 0.72 at a depth of 235 μm , with the most rapid increase taking place in the first 100 μm . The relationship between this particle volume fraction gradient and optical absorptance is investigated using an analytical model, which shows that depth-averaged absorptance measurements can measure the predicted average value, but will fail to capture local effects that result from a changing powder density. The time-averaged absorptance remains at levels between 0.67 and 0.80 across a two orders of magnitude range in laser power, which is significantly higher than that observed in solid stainless-steel experiments. The dynamic behavior of the absorptance, however, reveals physical phenomena, including oxidation, melting, and vapor cavity (keyhole) formation, as well as quantifying the effect of these on the absorbed energy.

DOI: [10.1103/PhysRevApplied.13.024057](https://doi.org/10.1103/PhysRevApplied.13.024057)

I. INTRODUCTION

The physical mechanism that underpins the initiation of the laser powder-bed additive manufacturing (AM) process is the interaction of an intense laser beam with a thin layer of metal powder on a substrate. This interaction is parameterized by the powder absorptance, which relates the amount of delivered laser-light energy to the amount of absorbed energy that can heat, melt, and even vaporize the material. Because of these physical effects, it is an inherently dynamic quantity, which is driven by the transition from an unperturbed powder through melting and vapor cavity (keyhole [1]) formation. Accurate measurements of absorptance are vital for thermophysical models that aim to understand and guide industrial laser material processes [2]. Absorptance is defined by

the *Commission Internationale de l'Eclairage* (International Commission on Illumination, CIE) as the “ratio of the absorbed radiant flux or luminous flux to the incident flux under specified condition [3].” Strictly speaking, it is not an intrinsic material property, as it relies on the external quantity of radiant flux [4]. The term absorptivity is described similarly mathematically and is commonly found in the literature to describe the results of similar measurements, but its definition is a thickness-dependent property [3]. Therefore, we prefer absorptance for powder layers, where powder layer thicknesses will influence the result.

Laser absorption by metal powder beds is extensively investigated with computational modeling. Most approaches use some form of a ray-tracing algorithm, in which the laser beam is treated as a collection of individual rays being reflected and absorbed by a metal particle with bulk optical properties [5–9]. The aggregate

*brian.simonds@nist.gov

of many rays is then used to calculate the net effect of the interaction. The powder-bed substrate is also a variable for these models, as the powder particle size [6,7,10–12], distribution [5,7,8,10,11], and thickness [6,7,9] will affect the optical absorption. Due to the computational complexity required in accounting for these parameters, spherical particles are typically assumed. These models are also used to investigate the effects of laser-power distribution [7–9], wavelength [5,13], and scan speed [14], as well as the effects of different solid absorptances [6,7,9] and mixtures of dissimilar powder materials [5,13,14].

Experimentally, absorptance in powder systems is measured using calorimetric [11,15–17] or optical [18–20] methods. Calorimetry-based approaches are attractive because measurements can be made under processing conditions similar to the AM process environment [15,21,22]. They measure the temperature rise of a material following a known amount of laser exposure, which is converted into optical energy absorption through the heat capacity that is typically estimated from literature values for bulk materials. However, calorimetry has a slow response time, and thus, only measures the average absorption, and under high laser irradiances on solid-metal targets, hot mass ejection can underestimate the absorbed energy [23]. Previous research has shown that hot mass can be ejected in powder systems as well [24,25], but its effects on calorimetry have not yet been investigated. Optical techniques measure reflected [18,20,26] or transmitted [19] light from a powder distribution. These previous experiments have mostly been performed with relatively low powers (below particle melting point) [18–20,26] or using powder targets that are not representative of those of created during the powder-spreading process involved with AM [18,19].

Here, we measure the absorptance of a thin powder layer prepared in a manner representative of laser powder-bed fusion AM using an integrating sphere method that calculates absorptance from the energy balance between the incident light and the total scattered light [23]. The powder is characterized with x-ray computed tomography (XCT) to determine powder particle locations, size and shape distributions, and porosity. The absorptance is measured for a single laser pulse with a duration similar to laser dwell times used in AM. We combine the results of the powder distribution with optical absorptance using the model developed by Gusarov and Kruth [13], which shows that the local absorptance drastically changes over the range of particle volume fractions measured. Our study spans two orders of magnitude of laser power, which allows for the observation of oxidation, melting, and vapor cavity (key-hole) formation and their absolute effects on laser-energy absorption. Lastly, we discuss measurement uncertainty, including a discussion of the possible effects of the vapor plume on our measurements.

II. EXPERIMENTAL METHODS

A. Dispersed and as-spread powder measurement and analysis

Argon-atomized 316L stainless-steel powder (LPW Technology Limited, 316AR-AABA, lot UK80026) [27] is used for all experiments. Its chemical composition is measured at a certified testing laboratory (Luvak, Inc.) [27] and the results are provided in Appendix A. Selected powder samples are further analyzed using XCT to obtain the powder size and shape distribution from a dispersed powder and to determine the as-spread powder configuration during optical measurements.

Determination of powder size distribution with XCT has been described in detail elsewhere [28–30]. Briefly, a powder is manually dispersed in a quick-setting epoxy, such that the volume fraction of powder in the powder-epoxy composite is approximately 10%, ensuring that powder particles are not touching, yet there are still enough for statistically valid analysis. The epoxy-powder mixture is drawn into a 3-mm-diameter rigid plastic tube using a small vacuum pump. After the epoxy has hardened, a 50-mm-long section is placed upright into a Zeiss Versa XRM500 XCT system [30] and scanned using a cubic voxel edge length of $0.8036\ \mu\text{m}$. Two fields of view (FOV) are obtained with roughly one thousand images captured in each (1000×1000 pixels) FOV.

Segmentation of the XCT reconstructed images into binary images is performed using a single threshold, where particles are white and the epoxy is black. Then, NIST-developed software is used on each set of images to identify individual particles. Only particles with a volume of at least 512 voxels (8 voxels across the particle) are analyzed, as particle shape cannot be accurately determined at smaller volumes [28,31]. Each analyzed particle is labeled and stored in a database, along with its three-dimensional (3D) image. Three-dimensional geometric information is recorded for each particle, including volume, length L , width W , and thickness T . A numerical search finds L , which is the longest length across the particle; W is the next longest length, but also perpendicular to L . Lastly, T is the longest length that is perpendicular to both L and W [30]. By this construction, $T \perp W \perp L$ and $T \leq W \leq L$. The three aspect ratios, L/T , W/T , and L/W , are useful for general particle classification, in particular, L/T . Using the values of L/T , along with visual inspection of the 3D images for a subset of particles, particles are separated into two classes: single nearly spherical (SnS) and highly nonspherical (NS) particles. Most, but not all, of the NS particles are smaller particles joined together [31]. When going through the segmented images, the programs also determine each particle's porosity.

XCT is also used to determine the geometrical distribution of the powder bed prepared in a similar manner to the “as-spread” condition used in the absorptance

measurements. An aluminum sample holder with high x-ray transparency is prepared, with a powder channel of $233.7 \pm 8.6 \mu\text{m}$ deep and approximately 4.1 mm long by 3.3 mm wide. The actual volume of this channel is determined by high-resolution optical profilometry to be $(3.31 \pm 0.06) \text{mm}^3$. Powder is spread using a metal blade, so that the measured distribution is representative of that used during the absorptance measurements. Although the depth of this channel is nearly the same as that used in the absorptance measurements, the other dimensions are much smaller, which is necessary for adequate x-ray transmission. Since the length and depth are orders of magnitude larger than that of the mean powder particle size, it is large enough that edge effects on particle distribution are negligible. For these measurements, the x-ray tube is set to 160 kV, 10 W of power, and a high-pass filter blocks lower energy x-rays to improve transmission. The instrument takes an interior scan of the powder; the aluminum walls are omitted in the reconstruction process. There is a slight angle (1.75°) between the incident x-ray beam and the base of the sample holder, which leads to a slope of the measured powder surface of the same amount.

This technique produces images of 984×1010 pixel, with a pixel and voxel size of $1.273 \mu\text{m}$. There are 264 total XCT images for the entire powder-bed height. Figure 1(a) shows the original reconstructed XCT image near the middle of the powder bed. Each image has a perfect circle fitting within the rectangular image, which cuts through perimeter particles, that is a mathematical artifact of the interior scan reconstruction algorithm. The gray background between the particles is another artifact of the scanning and reconstruction process; the space between particles is air and should be nearly black. Since several particles contain interior pores, all images are segmented, so that only grayscale powder and black porosity are seen, allowing for powder packing alone to be measured. A simple grayscale threshold does not work, as it leaves hole artifacts in the middle of particles. Therefore, we develop a 3D watershed process [32] because commercially available packages are only suitable for 2D images.

The 3D algorithm used for image analysis of the as-spread powder is adapted from that used for the dispersed powder images. In the dispersed powder, the 3D microstructure is already binary, so the algorithm only needs to find a single white powder voxel and then all directly adjacent white powder voxels. In contrast, for the as-spread powder, the algorithm starts on the outside of the 3D image, in the black exterior voxels, and then searches for all connected voxels that have a grayscale less than or equal to a threshold value (G) defined by the product of a parameter P , where $0 < P < 1$, with the maximum grayscale (G_{max}) found in the entire image set ($G = PG_{\text{max}}$). When this algorithm finds such a voxel, connected to a previously found voxel, it changes its grayscale to some arbitrary negative number. Once all voxels are

found, those with negative grayscales are turned black and the remaining gray voxels represent packed particles. By starting on the outside of the 3D image and working in, the particle interiors remain unchanged, unless they have perimeter grayscale values less than or equal to G . The particle volume fraction (PVF), or the ratio of volume containing metal versus the total volume, is defined inside a cylinder, the diameter of which is slightly smaller than that of the circular portion of Fig. 1(c). This is done to avoid edge effects from particles artificially cut by the visualization algorithm. Figure 1(b) shows the PVF achieved as a function of P .

The appropriate value for P is determined by independently measuring the apparent powder density (APD) of the as-spread powder bed and dividing by the density of bulk stainless steel. The APD is the mass of the as-spread powder divided by the volume in which it is spread [33]. Other methods of measuring the APD, such as the Arnold apparent density method [34] or the very high accuracy method developed by Jacob *et al.* [35], use volumes with much thicker powder layers than those we use here. As a result, these APD values would not be representative because gravity, mechanical vibration, and particle motion lead to additional settling. The mass is carefully measured in the sample XCT holder using a commercial scale with $1 \mu\text{g}$ readability (smallest detectable change in mass). This result, combined with the sample holder volume determined previously, give an APD of $(4.17 \pm 0.11) \text{g/cm}^3$, with the uncertainty due to the standard deviation from more than 10 measurements. This APD divided by the accepted room-temperature value for the density of 316L stainless steel (7.95g/cm^3 [36]) yields a measured PVF of 0.52 ± 0.01 . We then choose $P = 0.524$, such that the image-based analysis of PVF also results in a value of 0.52. If we estimate the uncertainty in P as ± 0.01 , then the uncertainty in the image-based PVF is the slope of the fitted line in Fig. 1(b) (2.97) multiplied by 0.01 to give 0.03. Therefore, the average image-based determination of the PVF is 0.52 ± 0.03 .

B. Integrating sphere measurements

The dynamic absorptance is measured using an integrating sphere with calibrated photodetectors to record the time-dependent reflectance (regular and diffuse [3]) during the entire laser pulse. This method, and a complete description of the instrumentation used, is detailed in a previous publication [23]. A schematic of the experiment is shown in Fig. 2 and a brief description is given here. The powder is spread with a metal blade in a stainless-steel sample holder with a 1 cm wide and $(195.8 \pm 5.5) \mu\text{m}$ deep trench. Figure 2 also shows a SEM micrograph of the top surface of the as-spread powder before it is exposed to laser irradiation.

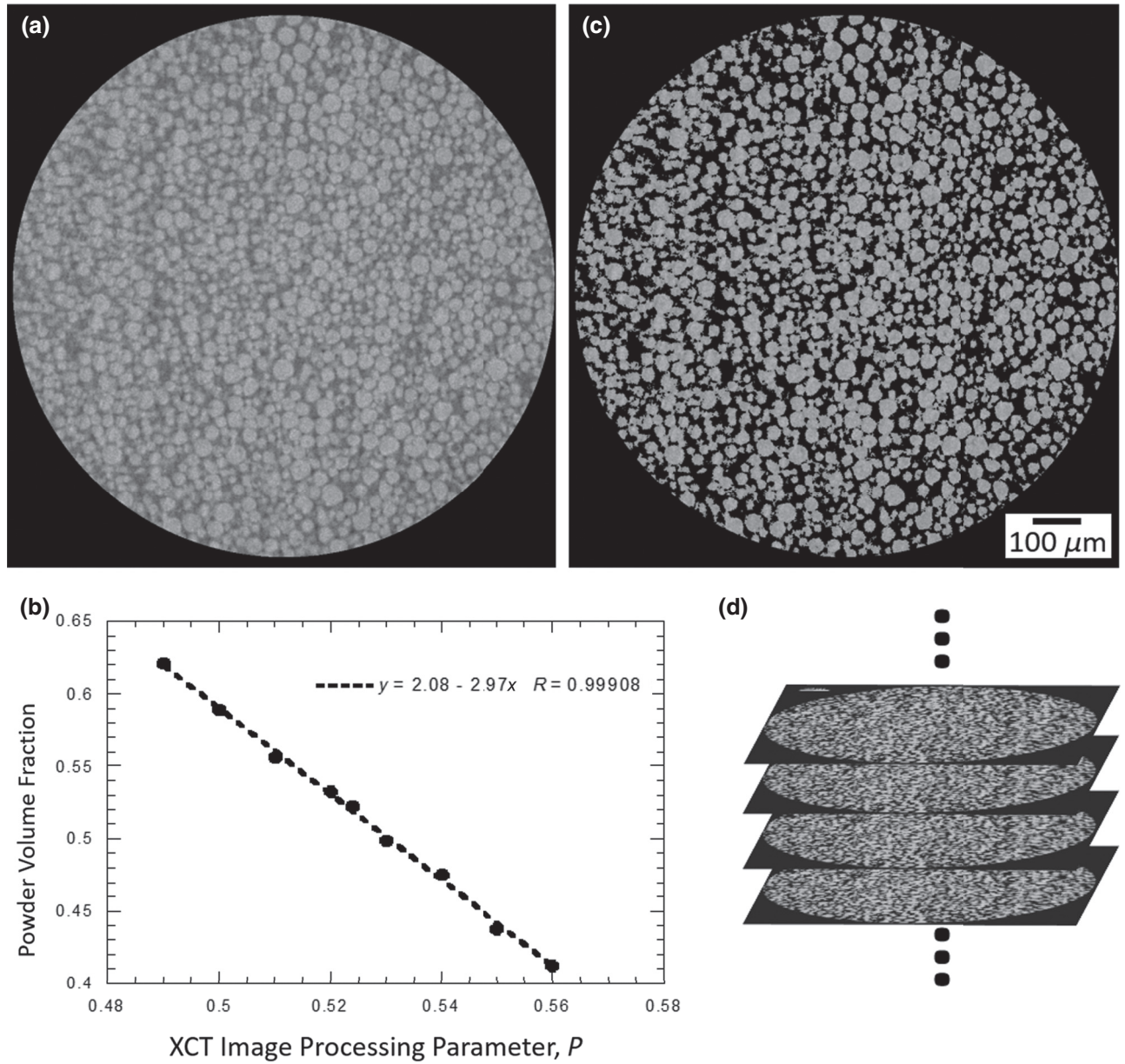


FIG. 1. XCT results of the spread powder. An original reconstructed image from roughly the middle of the powder volume is shown in (a). The calculated powder volume fraction as a function of the processing parameter, P , is shown in (b). The processed version of the image in (a) is shown in (c) with the appropriately chosen P . The image in (d) shows how these processed images are then stacked vertically to generate a three-dimensional volume rendering of the spread powder.

The time-dependent absorbed power, $P_{\text{absorbed}}(t)$, is computed by subtracting the measured absolute scattered light from the incoming laser beam according to

$$P_{\text{absorbed}}(t) = P_{\text{laser}}(t) - [P_{\text{head}}(t) + P_{\text{sphere}}(t)]. \quad (1)$$

The total scattered light is determined by adding the light scattered within the integrating sphere [$P_{\text{sphere}}(t)$] with the light directly back-reflected towards the incident laser beam [$P_{\text{head}}(t)$]. When these are integrated with respect to time, the corresponding energies are calculated. For

instance, the time integration of $P_{\text{absorbed}}(t)$ is the total absorbed energy (E_{absorbed}). Therefore, an average coupling efficiency, η_{coupling} , is computed according to

$$\eta_{\text{coupling}} = \frac{E_{\text{laser}} - (E_{\text{head}} + E_{\text{sphere}})}{E_{\text{laser}}} = \frac{E_{\text{absorbed}}}{E_{\text{laser}}}. \quad (2)$$

The pulse energy, E_{laser} , is calculated from an average of 10 laser pulses, which have a standard deviation of between 0.1% and 0.2% for all energies used in this study. The laser

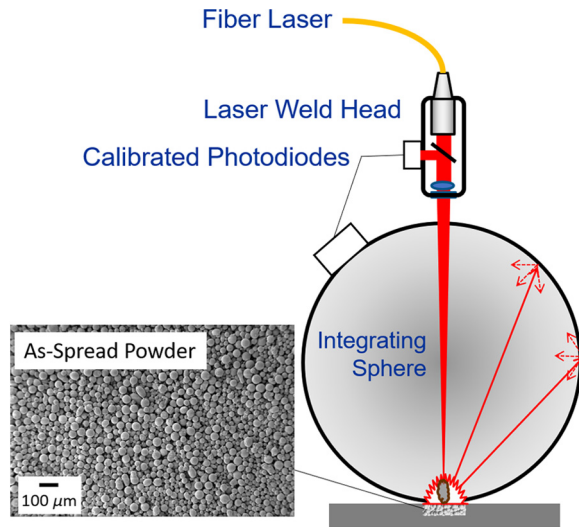


FIG. 2. A schematic of the light-scattering apparatus and analysis used in these experiments.

power as a function of time, $P_{\text{laser}}(t)$, is determined by separately measuring the laser-pulse temporal profile for every power setting, then scaling the time integral of this profile to equal the measured pulse energy, E_{laser} . The focused laser-spot spatial profile is sharply that of a top hat with a diameter ($1/e^2$) measured previously at $303 \mu\text{m}$ [23].

III. RESULTS AND ANALYSIS

A. Powder-bed analysis

Figure 3 shows a 3D rendering of the as-spread powder reconstructed from the XCT data depicted in Fig. 1(d). A virtual vertical slice at the bottom of the image is made to show the interior powder-bed structure. The 2D images

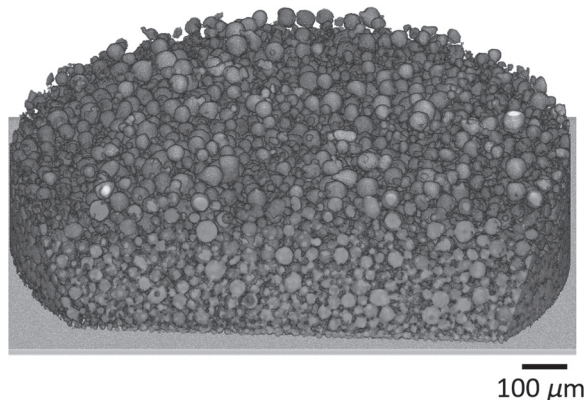


FIG. 3. Three-dimensional rendering of the powder bed from XCT measurements and analysis. There is a vertical slice through the bottom of the powder volume to reveal the powder particles below the surface. The reconstruction also shows the Al base of the powder holder.

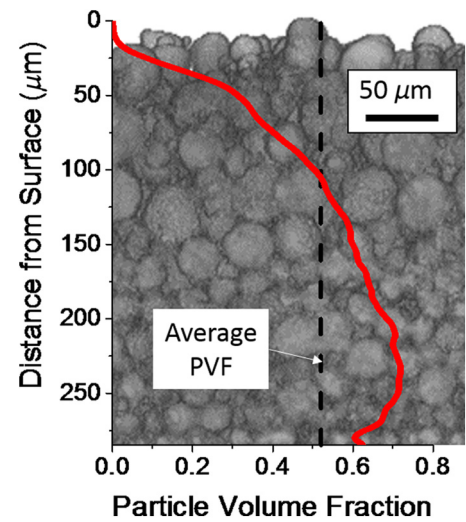


FIG. 4. The PVF versus the distance from the powder surface overlaid on a cross-sectional XCT image. The dashed line indicated the average PVF determined from the image analysis algorithm of the entire 3D structure.

used to create Fig. 3 can be found within the Supplemental Material [37]. In Fig. 4, we plot the PVF as a function of distance from the powder surface overlaid on a representative cross-section XCT image of approximately the same dimension in depth. The dashed line represents the volume-averaged PVF (0.52) determined using traditional techniques. There is a drastic reduction in the PVF as one approaches the powder surface, potentially caused by the settling of smaller particles lower in the powder layer to fill voids between larger particles. This is of particular importance for understanding laser-powder absorption, as this is dominated by the first $100 \mu\text{m}$ [20], and a single averaged value of the PVF will not accurately describe the powder distribution on this length scale. The small decrease in PVF near the substrate is due to a “wall effect,” where particles cannot pack as efficiently near a surface (within a few particle diameters) [38]. Notably, in Fig. 4, the decrease in PVF near the bottom surface starts at about $70 \mu\text{m}$ above the surface, which represents about twice the average value of the width, W (see Table I).

Table I summarizes the results from the dispersed powder XCT measurements for the average, volume-weighted dimensions and aspect ratios. The uncertainties on the L , W , and T measurements are $\pm 2 \mu\text{m}$, due to both image segmentation and the requirement that W , T , and L are perpendicular. Notably, most of the particles, 4426 out of 7208 (61%), are classified as SnS, while 39% are classified as NS. Figure 5 shows the particle size distribution based on the value of the 3D parameter W , which is chosen to represent particle “size,” as its value lies between those of L and T [39]. (An exception to this is for strongly nonspherical particles [40].) The y axis gives the volume fraction of the total amount of particles in a given bin. Figure 5(a) shows

TABLE I. Particle numbers, classifications, and average dimensional and aspect ratio data.

Particle	Number of particles	L (μm)	W (μm)	T (μm)	L/T	W/T	L/W
SnS	4426	30	28	27	1.12	1.06	1.06
NS	2782	62	40	34	1.82	1.18	1.55
All	7208	50	35	31	1.56	1.14	1.37

the distribution of all particles, whereas Fig. 5(b) plots SnS and NS particles separately, using similarly sized bins. For all three histograms, the bin heights and areas sum to 1.0.

Figure 6 shows the volume-fraction-based distribution of the L/T parameter using all particles. The long tail in Fig. 6 past $L/T = 1.3$ is mainly composed of particles consisting of two or more touching particles, with some irregular single particles. By the weight in the histogram in Fig. 6, there are clearly many of these particles by volume, in agreement with the results in Table I. Particle porosity is also determined from the XCT measurements, which are given in Appendix B, along with a comparison of the XCT-determined particle sizes with those from other measurements.

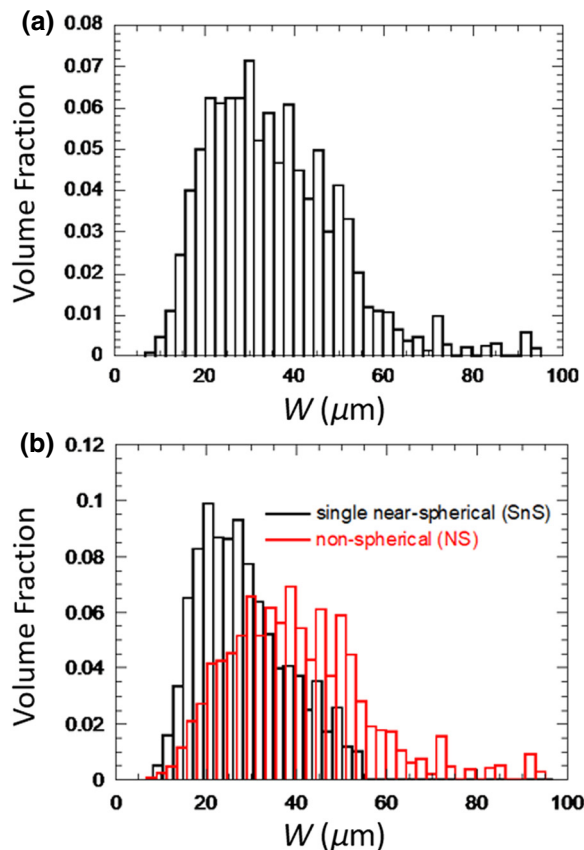


FIG. 5. Particle size distribution of particles using the width, W , as a measure of the particle “size,” in micrometers: (a) all particles combined and (b) SnS and NS PSDs computed separately, but displayed on the same graph.

B. Absorptance in the nonmelt regime

1. Integrating sphere results

The dynamic absorptance of a powder bed prepared in a similar manner as those used for the XCT measurements is measured optically with the integrating sphere apparatus. The lowest applied laser powers (region *A* in Fig. 9) result in a powder surface that does not show any discernable melting following laser illumination. This is observed with SEM imaging, as presented in Fig. 7(a) for the 11.7 W exposure. The red dashed circle illustrates the relative size of the focused laser-beam spot, but not necessarily its exact location. Optical images (not shown) reveal a slight discoloration at the powder surface at 11.7 W, but not at 1.93 W. Figure 7(b) shows $P_{\text{absorbed}}(t)$ for the two laser powers of region *A*. The initial rise and final fall of the signal follow that of the laser pulse. At 1.93 W, $P_{\text{absorbed}}(t)$ is constant at 1.44 W or 74.2% of the average input power ($\eta_{\text{coupling}} = 0.742$). [Notably, the data presented in Fig. 7(b) are multiplied by four, so that features are visible at this scale.] At 11.7 W, after the initial step rise that follows the laser rise time, there is a slight positive slope in $P_{\text{absorbed}}(t)$ of about 1 W/ms. Given that a slight discoloration in the powder is observed at this power, this is most likely to be due to increased absorption from oxidation during heating.

2. Relationship between particle packing and absorptance

Theoretical investigations of absorbed laser light by a powder-bed surface begin with either an assumed particle

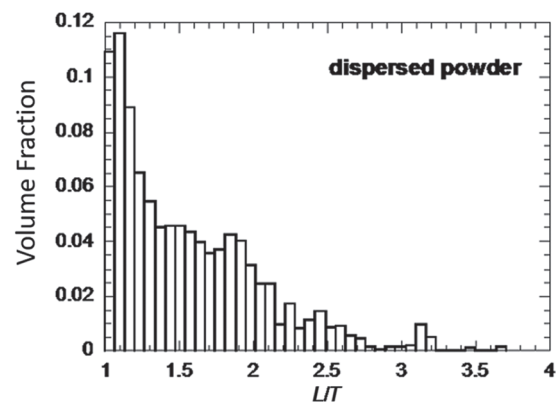


FIG. 6. Volume-fraction based L/T histogram for all particles combined.

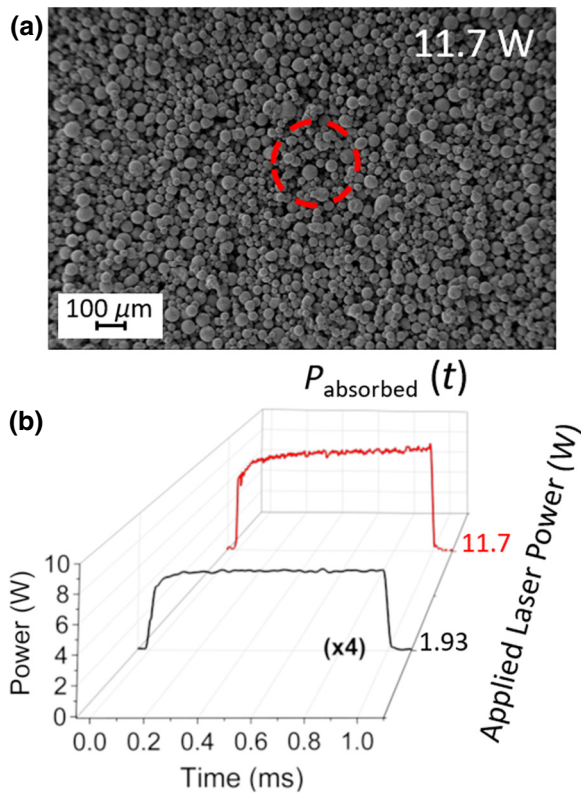


FIG. 7. (a) SEM micrograph after exposure to 11.7 W laser light for 1 ms. There is no visible melting, but some slight discoloration seen in optical images (not shown). (b) Absorbed laser power for very low powers (1.93 and 11.7 W), with the lowest power data multiplied by four, so that details are visible on this scale.

distribution based on a particular packing order [11,41] or a modeled distribution resulting from dropped particles [5,9,10,12]. In either case, the models typically use a single PVF value and assume spherical particles. The XCT measurements presented above show that our as-spread powder system has a rapidly changing PVF, especially over the first 100 μm, and many nonspherical particles. Therefore, most theoretical models that have been developed are not directly applicable to our system. One exception, however, is the study by Gusarov and Kruth [13], which numerically solved the radiation transfer equation for laser light incident to a thin powder layer on a reflecting substrate. This model is attractive for analyzing our results because it does not *a priori* assume spherical particles and is instead sensitive only to the powder layer porosity and the surface area of the powder particles facing these pores, both of which can be derived from the XCT measurements.

According to their model, the absorptance of a powder layer on a substrate is determined by the dimensionless optical thickness parameter, $\lambda = (1/4)SL$, where L is the depth of the powder layer. S is the specific powder surface area per unit pore volume, given as $S = \delta (1 - \epsilon)U\epsilon$,

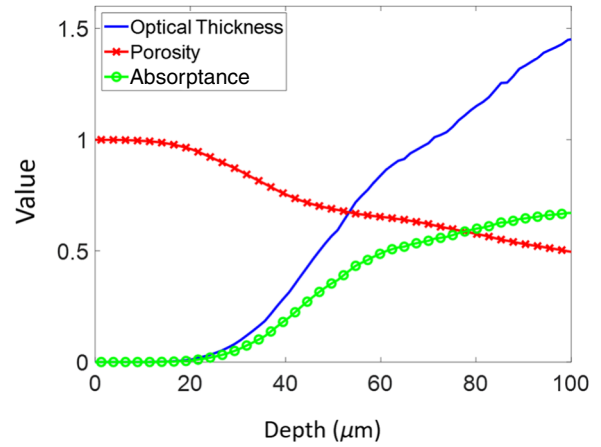


FIG. 8. The calculated optical thickness (blue line) and absorptance (green circles) plotted versus depth using the porosity (red crosses) measured at that depth for a 100 μm powder-bed layer.

where δ is the density of the bulk powder material ($\delta = 0.7$) and ϵ is the porosity of the powder layer. Notably, ϵ is not the individual particle porosity (discussed within the Supplemental Material [37]), but rather the ratio of empty space to the total volume of the powder layer or $(1 - PVF)$. U is the specific surface area or total surface area of particles per unit mass. The total particle surface area, A_{pore} , can be determined by analyzing each slice of the 3D XCT reconstruction [Fig. 1(d)] for the number of pixels at powder-pore interfaces and multiplying by the square of the pixel size, d . A correction factor of 4/6 is

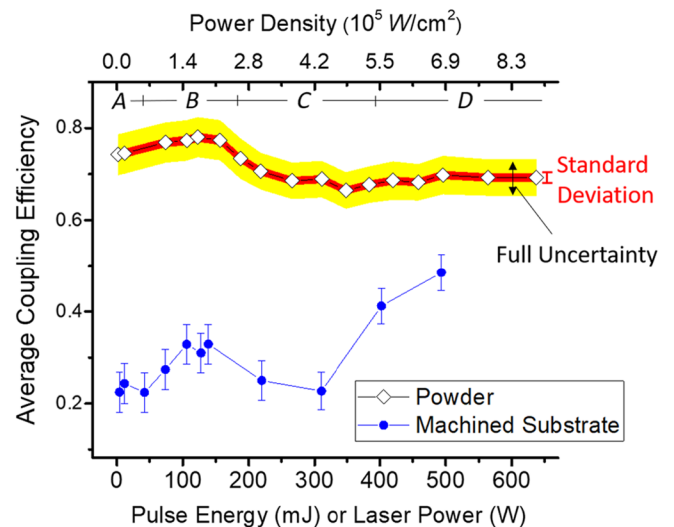


FIG. 9. Average coupling efficiencies of the stainless-steel powder and the bare machined substrate holder. The horizontal axis represents both the total energy in the laser pulse (mJ) and the average laser power (W). This equivalence comes from the injection duration of 1.000 ms.

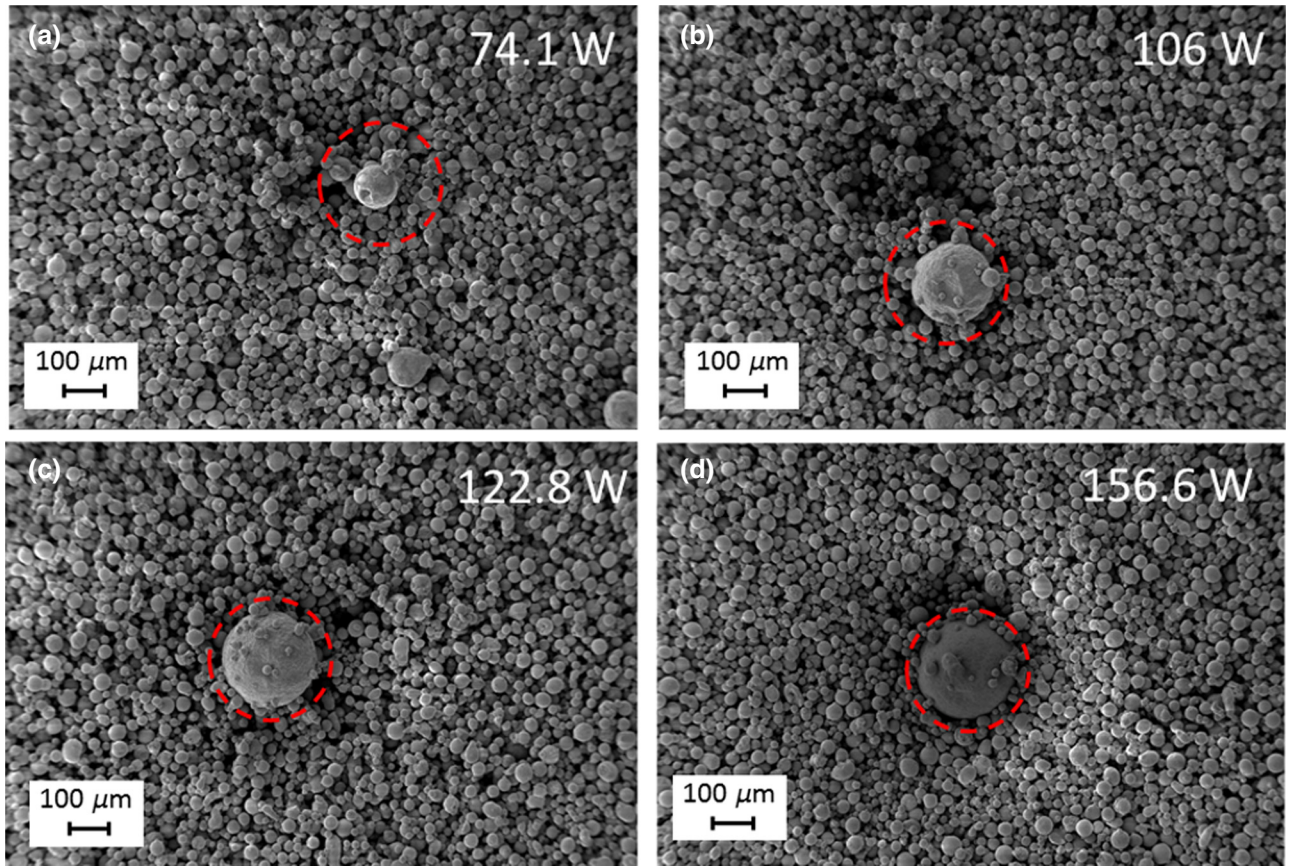


FIG. 10. SEM micrographs for laser powers that produce the onset of powder melting.

applied to A_{pore} that results when the surface area is determined from a pixelated volume [42,43]. The unit mass is the number of pixels containing a powder particle times a cubic voxel or the PVF times the total number of pixels in the slice, N_{pix} . With these definitions, we find that the optical thickness as a function of as-spread powder depth is

$$\lambda(z) = \left(\frac{L}{4}\right) \left[\frac{A_{\text{pore}}(z)}{N_{\text{pix}}d}\right] [1 - \text{PVF}(z)]. \quad (3)$$

This definition can then be used to calculate the absorptance as a function of depth, according to Eq. (45) in Ref. [13] (or Eq. (21) in Ref. [44]). The measured porosity and calculated optical thickness and absorptance are shown in Fig. 8 for $L = 100 \mu\text{m}$, which is a more typical AM powder-bed thickness. It is important to note that this is not an absorption profile through the powder layer, but rather the absorptance calculated with the PVF measured at each depth. As such, this illustrates how the calculated absorptance would change if the actual PVF at a particular depth were used. In addition, Ref. [13] showed that, as the thickness of the powder layer increases, the absorptance asymptotes to a single value, which is known as a deep powder-bed limit. In our calculations,

the absorptance asymptotes to 0.77, which is close to our experimentally determined value of $\eta_{\text{coupling}} = 0.742$ measured at the lowest laser power. The asymptotic behavior suggests that depth-averaged absorptance measurements of metallic powders can measure the correct average value, but will fail to capture local effects resulting from the gradient in powder density. For accurate calculations of local energy deposition, a model incorporating this more complex reality is necessary. Of course, for AM, this is only relevant for the initial time period of light-powder interaction because the melting powder presents an entirely different surface to the incoming laser beam.

C. Dynamic high-power absorptance

1. Average coupling efficiency

Coupling efficiencies, η_{coupling} , are plotted in Fig. 9 for the stainless-steel powder and, for comparison, the bare machined substrate averaged over the 1 ms laser pulse. The “laser power” referred to in Fig. 9 is that of measured E_{laser} divided by 0.001 s, which is reasonably close to the asymptotic value of $P_{\text{laser}}(t)$ given that the laser pulse is temporally square with a short $30 \mu\text{s}$ rise time to the 95% level. At low average power, the substrate has an average coupling efficiency between 0.2 and 0.3, which then rises

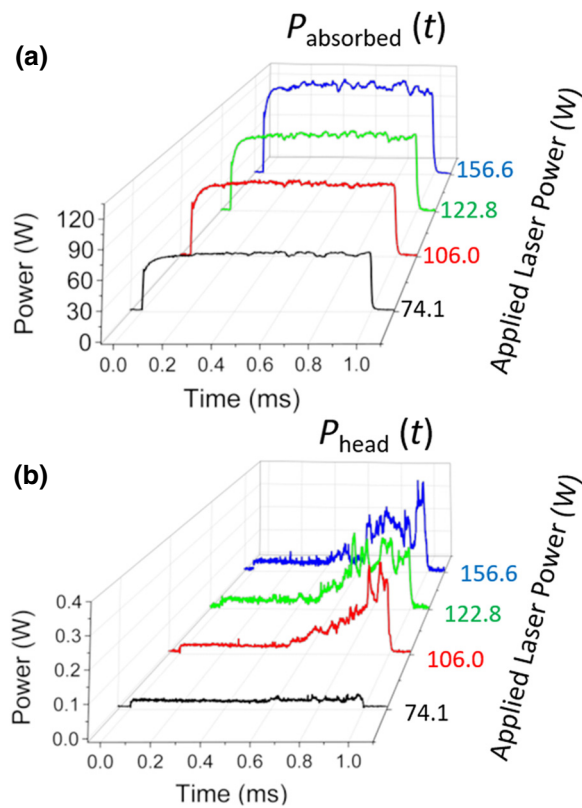


FIG. 11. Absorbed laser power (a) and directly reflected laser power (b) for incident laser powers that cause the onset of powder melting.

by almost a factor of two as the laser power goes from 300 to 400 W. This behavior was shown previously to indicate the formation of a recoil pressure-induced cavity (a keyhole) [23], which leads to increased absorption through multiple reflections. In contrast, the stainless-steel powder does not experience such a dramatic shift in coupling efficiency and remains between 0.67 and 0.80 over the entire power range.

These data are separated into four regions based on a physical interpretation of the dynamic absorptance. Region *A* is nonmelting, *B* is the onset of melting, *C* is full melt penetration, and *D* is where keyholing occurs. Also shown for the powder data are shaded regions, which indicate both the standard deviation and the full uncertainty of our measurements. The error bars for the machined substrate represent the full uncertainty.

2. The onset of melting

Region *B* in Fig. 9 is characterized by the appearance of a mass of large particles created by powder melting and solidification and which grows in size with increasing laser power to approximately that of the focused laser beam, as shown in Figs. 10(a)–10(d). Again, the red dashed circles indicate the relative size and approximate location of the incident laser beam. In Fig. 10(a), there are three particles

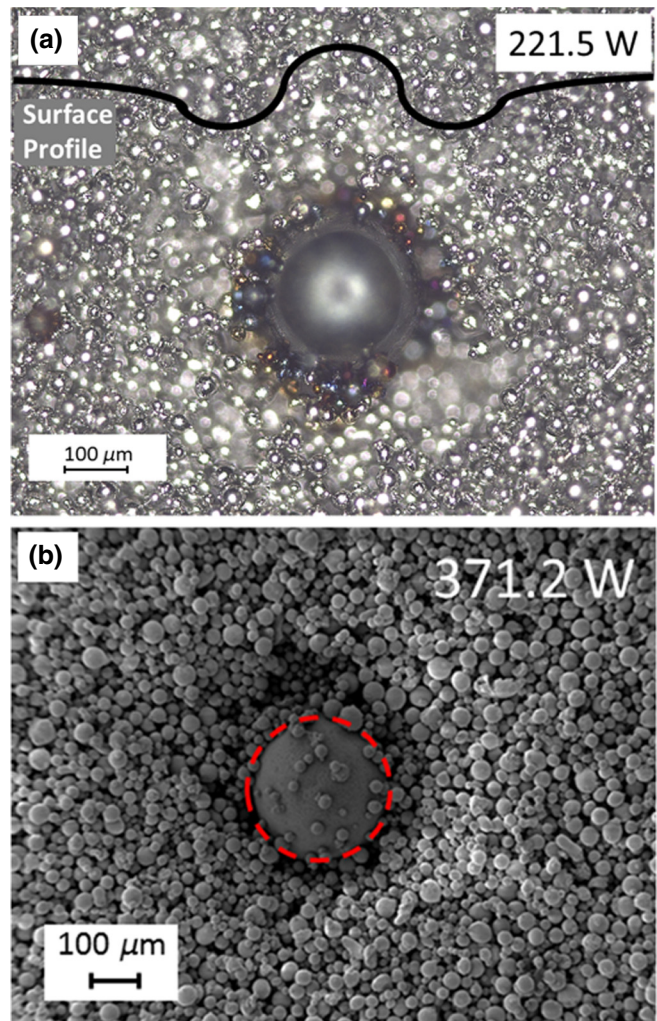


FIG. 12. (a) A confocal optical image of powder melted with 221.5 W laser light, with a sketch of the approximate surface profile determined by scanning the focal plane vertically. (b) A SEM micrograph of powder melted at 371.2 W.

that are much larger than the mean particle size and are presumed to be from particle agglomeration following melting and solidification. These are distributed over several hundreds of micrometers, which suggests that they result from an ejection process. Furthermore, it appears that there is a depression in the powder surface near the circled feature, which is further evidence of a dispersive force. As the laser power increases, the size of the metal bead also increases. In Fig. 10(b), a large depression in the powder surface is present near the bead, and in Figs. 10(c) and 10(d), the bead is concentric with the depression.

$P_{\text{absorbed}}(t)$ and $P_{\text{head}}(t)$ over this power range are given in Figs. 11(a) and 11(b), respectively. Interestingly, the dynamic absorbed power is relatively constant with only small variations. The onset of melting seen in the SEM images is accompanied by increased variability in $P_{\text{absorbed}}(t)$, as compared with that in Fig. 7. Furthermore,

there is additional evidence of melting in $P_{\text{head}}(t)$, which now has a resolvable signal, albeit one with an absolute power that is significantly lower than $P_{\text{sphere}}(t)$. The sharp increase in $P_{\text{head}}(t)$ is a clear indication of melting, as the molten metal is much more reflective than the bare powder. Also telling is that the rapid rise in $P_{\text{head}}(t)$ occurs at increasingly earlier times, as the applied laser power is increased. These interpretations, and those to follow, are consistent with the analysis from solid stainless steel [23].

3. Full melt penetration

Region *C* in Fig. 9 shows a subtle decline in the coupling efficiency, since the laser beam is mostly incident to a reflective molten metal pool for most of the 1 ms exposure. Visual observations of the processed surface show that the diameter of the metal bead does not grow much beyond the approximate size of the focused laser-beam spot (Fig. 12). However, these metal beads remain welded to the substrate once the powder is gently removed from the holder. This is not true for the beads formed in region *B*. Figure 12(a) is an optical microscope image of a bead formed with 221.5 W, which has a shallow depth of focus. Therefore, it is a useful image for determining the relative height of the observed features. In this image, the surface of the untouched powder is at the focal plane and the out of focus areas are either above or below. By translating the microscope objective through the focal plane, we find that the surface of the bead is above the surface of the powder and the out-of-focus annular ring around the bead is below. The dark solid line at the top of the image in Fig. 9(a) approximates this topology. This is believed to be a result of denudation, which has been widely reported for AM processes [45,46]. A SEM micrograph taken at 371.2 W is given in Fig. 12(b).

Another feature of note in Fig. 12(a) is the presence of colored oxidized powder beads directly around the large central bead. The different colors result from varying thicknesses of oxide and appear not to have melted, as they are roughly the same diameter as that of the original powder particles. [This premelt oxidation is the cause of the slight increase in $P_{\text{absorbed}}(t)$ seen in the sample treated with 11.7 W in Fig. 7.] As these oxidized particles reached very high, but still sub-melting, temperatures, some are presumably ejected by the metal gas vapor creating the denuded zone [45].

Figure 13 shows $P_{\text{absorbed}}(t)$ and $P_{\text{head}}(t)$ for the data in region *C*. $P_{\text{absorbed}}(t)$ shows increased variability, but with a slight downward trend over the duration of laser exposure due to the increase in reflectivity of the melted powder. For example, measured from the peak value in the 383.8 W curve, $P_{\text{absorbed}}(t)$ has a slope of -20.9 W/ms. When integrated to find the average coupling efficiency, this negative slope helps to create the slight downward trend seen in Fig. 9, region *C*. Furthermore, $P_{\text{head}}(t)$ continues the trend from the previous region, where the onset of sharp signal spikes

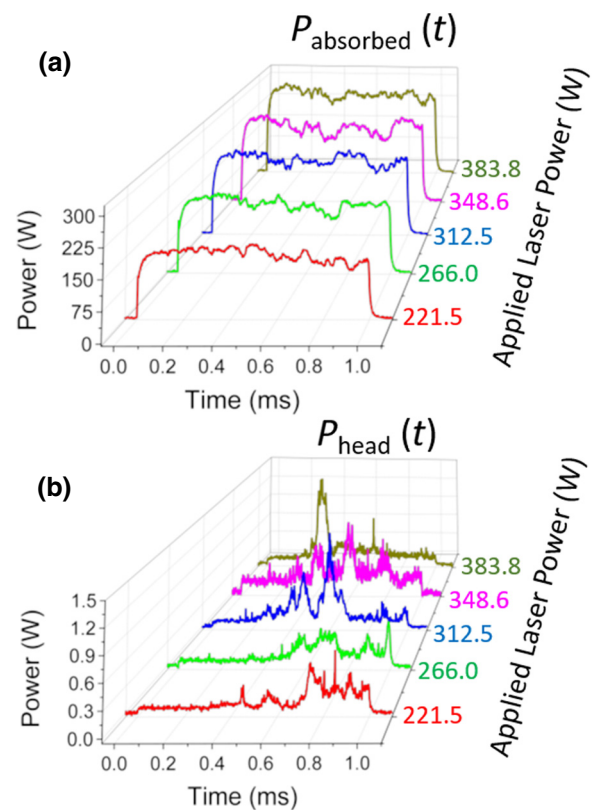


FIG. 13. Absorbed laser power (a) and directly reflected laser power (b) for incident laser powers that show melting and full powder penetration.

occurs at increasingly earlier times to indicate of the onset of melting.

4. Keyhole formation

As the average laser power is increased further, the average coupling efficiency becomes constant across region *D*. Again, however, dynamic $P_{\text{absorbed}}(t)$ reveals additional information. The trends in $P_{\text{absorbed}}(t)$ and $P_{\text{head}}(t)$ can be seen in Figs. 14(a) and 14(b), respectively. With increasing laser power, the slight downward trend in $P_{\text{absorbed}}(t)$ seen in Fig. 13(a) is reversed, until a clear increase in $P_{\text{absorbed}}(t)$ appears. In fact, the time-dependent behavior of $P_{\text{absorbed}}(t)$ at the highest applied power of 637.1 W is qualitatively similar to that seen in a solid metal when a keyhole is formed [23]. Thus, in powder, there is an initial peak in $P_{\text{absorbed}}(t)$ due to solid-state heating, followed by a decrease due to melting with a longer-term increase representing keyhole formation and growth.

5. Uncertainty analysis and discussion

The full uncertainty in the average coupling efficiency is presented as the wider shaded region in Fig. 9 and represents a complete analysis of the systematic uncertainties associated with our measurement. Complete details of how

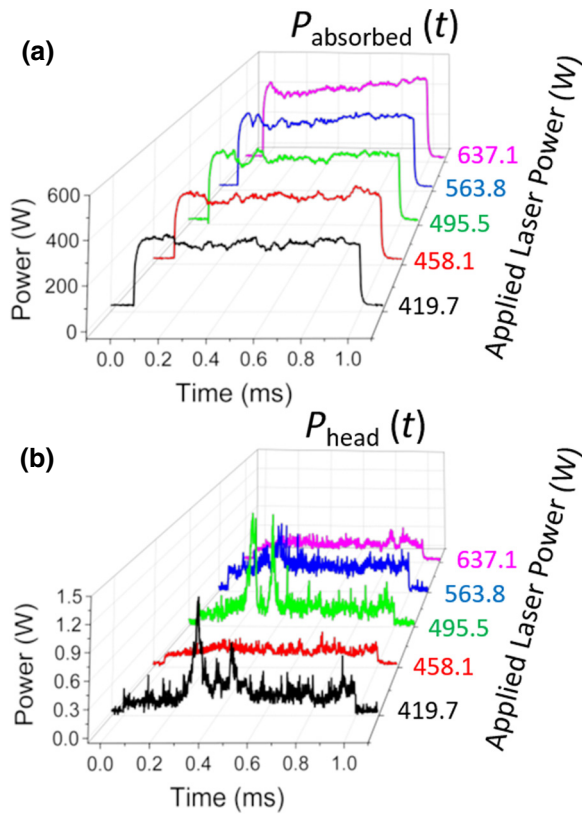


FIG. 14. Absorbed laser power (a) and directly reflected laser power (b) for incident laser powers that show signs of keyhole formation.

this is determined can be found in a previous publication [23]. The largest source of systematic uncertainty is from the laser power measurement device (3%), which will be a limitation common to any similar technique where the energy balance is determined by laser power measurements. Random uncertainties are determined by calculating the standard deviation associated with repeated measurements, which are shown as the narrow shaded region in Fig. 9. As an example, Fig. 15 shows repeated measurements at 221.5 W average laser power on fresh spots of the bare powder. Figure 15(a) gives $P_{\text{absorbed}}(t)$ and Fig. 15(b) shows the directly back-reflected laser power, $P_{\text{head}}(t)$. There is variability with respect to the timing of specific features, but they are qualitatively similar. Due to the time integration involved in determining η_{coupling} , this variability has a minimal effect, and the standard deviation of η_{coupling} is only 1.2%, relatively.

Our calculations currently neglect the effects of the vapor plume. Ultimately, these will be difficult to quantify due to its complicated and time-dependent nature, but we can estimate its effect on our measurements with the following analysis. We consider that the vapor plume consists primarily of molten metal droplets [24], entrained solid powder particles [45], and neutral atomic metal vapor [47]. In our analysis, we neglect the presence of a plasma,

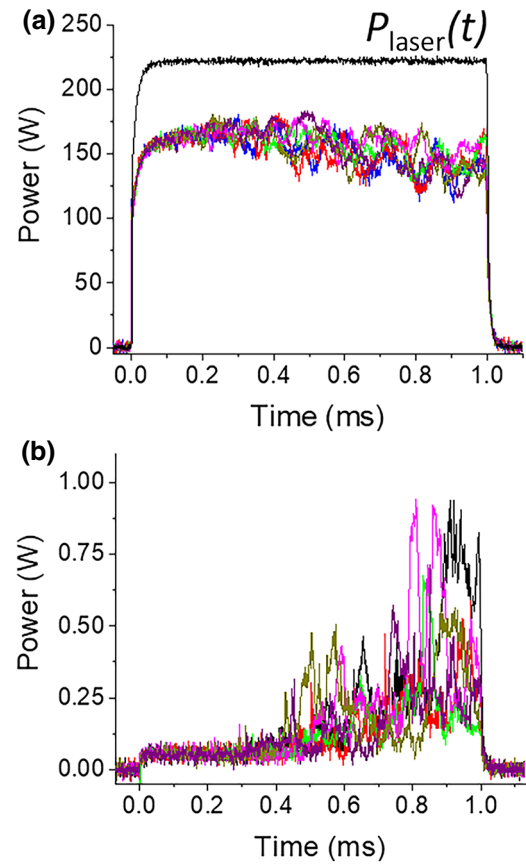


FIG. 15. Repeated measurements of (a) $P_{\text{absorbed}}(t)$ (multicolored curves) and the laser pulse profile, $P_{\text{laser}}(t)$ (black), and (b) $P_{\text{head}}(t)$ to show the repeatability of the measurement technique.

as there is substantial evidence that ionized atoms do not exist in an appreciable amount to cause significant inverse Bremsstrahlung absorption at the 1 μm wavelength [47–51], and spectral measurements during AM processes show only neutral atomic spectral lines [52–55]. These data suggest that the bright light observed during laser welding or AM is largely a result of incandescence from a hot metal gas. On a timescale relevant to this work, atomic metal atoms (iron) are seen in the vapor plume with laser-induced fluorescence during intense laser irradiation of stainless steel [56]. Metal atoms will only absorb incoming laser light if those atoms have an allowed optical resonant transition in the wavelength range of the laser. For resonances between 1065 and 1075 nm, there are no allowed optical transitions for the major atomic constituents in 316L stainless steel (Fe, Cr, Ni, Mo, Mn) [57].

Furthermore, many studies have shown that the vapor contains metal particles over a very large size distribution. The interaction of the laser beam with particles is explained by Mie theory and can be absorptive, reflective, or both, as determined by the particle size [48]. The largest particles considered here are the molten metal droplets and entrained powder particles that have dimensions on

the order of 10 μm . As this is large with respect to the laser wavelength (1.070 μm), these particles are mainly reflective. This scattered laser light will contribute to the measured sphere signal [$P_{\text{sphere}}(t)$] as unabsorbed radiation and is therefore accounted for. (This contrasts with calorimetric methods, for instance, where this contribution would be completely unaccounted for.)

Studies during laser welding have found that the plume can contain smaller nanoparticles in the range of 10–100 nm [49,58,59]. The smaller size of these particles means that absorptive processes can be much more significant. Measurements of attenuation of the laser by the plume during the AM process are scarce; instead, several studies have been performed during laser welding. However, these studies occur under orders of magnitude higher irradiances ($>1 \text{ MW/cm}^2$) and much longer laser dwell times than are typical for AM. An early work by Greses *et al.* reported attenuation as high as 40% during continuous 8 kW laser welding [49], which remains considerably higher than that of subsequent reports. Under extremely high irradiation of 20 kW, Shcheglov *et al.* later reported a high laser-beam attenuation of 12% [51]. Zou *et al.* calculated that the absorption of the plume produced by 7 MW/cm^2 illumination was a strong function of plume height and that plumes on the order of millimeters (like those in our experiments) should only absorb about 1% of the incoming laser light [59]. Katayama *et al.* measured a 3% attenuation of a probe beam, but this was reached only after 1 s of laser exposure [60]. A high-speed video of their plume shows that after 2 ms of laser exposure the plume is significantly smaller than that at later times.

Similarly, Scholz *et al.* found that multiple probe beams through a laser welding plume were not attenuated until several milliseconds after illumination began, suggesting a rate of nanoparticle formation in the plume that was longer than that of the 1 ms exposure of our experiments [58]. Furthermore, in our experiment, an absorption by metal vapor amounts to subtracting E_{laser} in Eq. (2) by the amount of energy absorbed by the plume. If we were to conservatively assume 3% absorption of the incident laser light when the integrating sphere measured that 30% of the incident light was scattered, the absolute effect on the calculated coupling efficiency would be an overestimation of 0.9%. Therefore, although we cannot definitively claim that the metal vapor plume is not absorbing some of the incoming laser light, we believe that its effect is small (less than 1%) because of the very short duration of the pulses, the lower irradiances used, and the relatively modest plume heights under our experimental conditions.

IV. CONCLUSIONS

We measure the dynamic absorptance of focused laser light incident to a metal powder-bed surface, the geometry of which is determined using XCT. The reconstructed

XCT data provide a three-dimensional analysis of the spread powder, in terms of powder particle location, size and shape distribution, and porosity. This gives the initial preirradiated condition of the spread powder, on which the absorptance measurements are performed. These measurements reveal that the particle volume fraction changes significantly over the depth of interest ($<100 \mu\text{m}$) for light absorption. Furthermore, by applying the results of a numerical model for the absorptance, we find that, over this depth range, the absorptance is strongly determined by the particle volume fraction. Therefore, the local energy absorption at particle surfaces will be affected, even though the measured depth-averaged value agrees with that predicted. The dynamic absorptance measurements also observe physical changes to the powder system, such as oxidation, melting, and keyhole formation, while the time-integrated coupling efficiency changed little as a function of incident laser power. This underscores the importance of using time-dependent energy-coupling values for high-fidelity AM model validation that aim to predict defects due to changes in melt pool behavior, as these features are only apparent dynamically.

ACKNOWLEDGMENTS

The authors are grateful to Brandon Lane and Jake Benzing for their careful reading of the manuscript and insightful comments. This article is a contribution of the U.S. Government, not subject to U.S. copyright.

APPENDIX A: POWDER COMPOSITION

Table II shows the elemental composition of the stainless steel powder used in these experiments and compares the manufacturer's specification with separate results from inductively coupled plasma measurements.

APPENDIX B: PARTICLE SIZES AND POROSITY

We compare the results of L , W , and T analysis to other powder distribution measurements made with

TABLE II. Powder composition from manufacturer and inductively coupled plasma (ICP) measurements [61].

Element	Manufacturer specifications	ICP measurements
Fe	Balance	Balance
Cr	16.92	16.25
Ni	12.06	11.45
Mn	1.21	1.15
Si	0.63	0.56
Mo	2.50	2.40
C	<0.01	0.009
S	0.005	0.005
N	0.01	0.01
P	<0.005	0.005
O	0.05	0.05

TABLE III. Values of $D10$, $D50$, and $D90$ for laser-diffraction, L , W , T , and VESD measurements.

Size measurement	$D10$ (μm)	$D50$ (μm)	$D90$ (μm)
Laser diffraction	20.1	32.4	51.3
L	21.0	44.2	86.5
W	18.9	33.4	53.2
T	17.3	30.1	46.0
VESD	18.2	32.4	49.2

laser-diffraction particle size measurements [61,62]. The simplest comparison is with the values of D_n , where n is 10, 50, and 90. D_n is the particle size at which $n\%$ of the particles, by mass or volume, have sizes smaller than that of D_n . Previous laser-diffraction particle size distribution measurements [61] give a range of particle sizes in terms of sphere diameters, with a certain volume fraction per size bin, that give equivalent light scattering to the real particles. The volume equivalent sphere diameter (VESD) is the sphere diameter resulting in a volume equivalent to that of the measured nonspherical particle. We determine L , W , T , and VESD for the particles, and thus, we can compute $D10$, $D50$, and $D90$ for each size measurement. The results are given in Table III, where there is no precise agreement among the four parameters derived from XCT measurements and the laser-diffraction results. The values of $D10$, L , W , and VESD agree with the laser-diffraction results within the XCT uncertainties, $\pm 2 \mu\text{m}$. However, only W and VESD agree with the laser-diffraction results within the uncertainty for $D50$ and $D90$. This is because laser-diffraction analysis assumes spherical particles, which XCT reveals to be largely not true. To be clear, the spherical interpretation of the laser-diffraction measurement is not the same as the VESD interpretation, and L , W , and T measure different aspects of nonspherical particle dimensions. Therefore, for a complete understanding of the as-spread powder system, a single value for particle size is misleading.

Some of the particles contain pores that are detected by the XCT scans and the numerical processing of the segmented images. Table IV shows a summary of the porosity values, in terms of the number of particles containing internal pores, the average porosity per porous particle, and the maximum value of porosity found. The porosity can be conceptualized in the following way. A spherical particle of $35 \mu\text{m}$ in diameter (see W in Table IV) would have a volume of $22\,450 \mu\text{m}^3$. At an average value of porosity of 0.8% , the pore volume would therefore be $180 \mu\text{m}^3$, which,

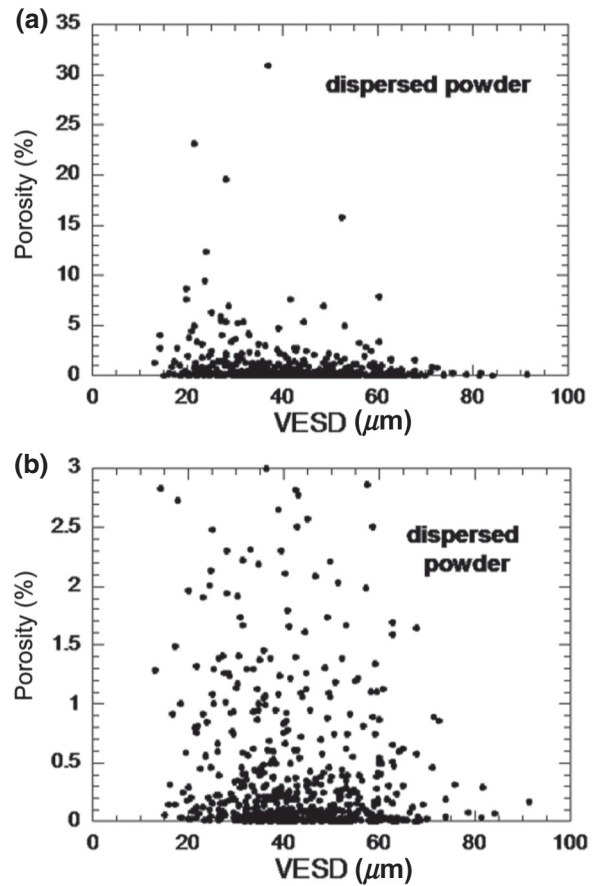


FIG. 16. Porosity of each porous particle plotted versus the VESD of each particle: (a) all particles and (b) those particles with porosities below 3%.

if concentrated into a single spherical pore, would have a diameter of $7 \mu\text{m}$. However, at the maximum porosity of 31% , this hypothetical single spherical internal pore would have a diameter of $24 \mu\text{m}$, which is more than $2/3$ of the particle diameter.

Figure 16 shows a graph of the porosity of each porous particle plotted as a function of VESD. Figure 16(a) shows all particles and Fig. 16(b) shows those with a porosity below 3% to better visualize the smaller porosity data. The porous particles are evenly distributed over the full size range, as estimated by VESD, with perhaps a slight trend towards lower porosities for the largest particles. This result may imply that the prevalence of pores and pore size are similar, irrespective of particle size, so that larger particles have similar pore volumes to those of smaller particles, and therefore, lower porosities. Certainly, Fig. 16(a)

TABLE IV. Internal porosity summary statistics for all particles.

Number of particles with internal pores	Fraction of particles that had internal pores (%)	Average porosity per porous particle (%)	Maximum porosity found (%)
621	8.6	0.8	31

shows that the highest porosities, more than 5%, are concentrated in the smaller sized particles.

-
- [1] W. E. King, H. D. Barth, V. M. Castillo, G. F. Gallejos, J. W. Gibbs, D. E. Hahn, C. Kamath, and A. M. Rubenchik, Observation of keyhole-mode laser melting in laser powder-bed fusion additive manufacturing, *J. Mater. Process. Technol.* **214**, 2915 (2014).
- [2] R. Indhu, V. Vivek, L. Sarathkumar, A. Bharatish, and S. Soundarapandian, Overview of Laser Absorptivity Measurement Techniques for Material Processing (2018).
- [3] CIE, *DIS 017/E:2016 International Lighting Vocabulary* (CIE Central Bureau, Vienna, Austria, 2016), 2nd ed.
- [4] M. F. Modest, *Radiative Heat Transfer* (Elsevier Inc., Oxford, UK, 2013), 3rd ed.
- [5] X. Wang and J. Kruth, in *Comput. Tech. Mater. Compos. Compos. Struct.*, edited by B. H. V. Topping (Civil-Comp Ltd, Edinburgh, 2000), pp. 57–71.
- [6] A. Streek, P. Regenfuss, and H. Exner, Fundamentals of energy conversion and dissipation in powder layers during laser micro sintering, *Phys. Procedia* **41**, 858 (2013).
- [7] D. Moser, S. Pannala, and J. Murthy, Computation of effective radiative properties of powders for selective laser sintering simulations, *J. Miner. Met. Mater. Soc.* **67**, 1194 (2015).
- [8] C. D. Boley, S. A. Khairallah, and A. M. Rubenchik, Calculation of laser absorption by metal powders in additive manufacturing, *Appl. Opt.* **54**, 2477 (2015).
- [9] X. Li and W. Tan, in *Proc. 27th Solid Free. Fabr. Symp.* (2016), p. 219.
- [10] J. Zhou, Y. Zhang, and J. K. Chen, Numerical simulation of laser irradiation to a randomly packed bimodal powder bed, *Int. J. Heat Mass Transf.* **52**, 3137 (2009).
- [11] C. D. Boley, S. C. Mitchell, A. M. Rubenchik, and S. S. Q. Wu, Metal powder absorptivity: Modeling and experiment, *Appl. Opt.* **55**, 6496 (2016).
- [12] H. C. Tran, Y. L. Lo, and M. H. Huang, Analysis of scattering and absorption characteristics of metal powder layer for selective laser sintering, *IEEE/ASME Trans. Mechatronics* **22**, 1807 (2017).
- [13] A. V. Gusarov and J. P. Kruth, Modelling of radiation transfer in metallic powders at laser treatment, *Int. J. Heat Mass Transf.* **48**, 3423 (2005).
- [14] X. C. Wang, T. Laoui, J. Bonse, J. P. Kruth, B. Lauwers, and L. Froyen, Direct selective laser sintering of hard metal powders: Experimental study and simulation, *Int. J. Adv. Manuf. Technol.* **19**, 351 (2002).
- [15] R. P. Martukanitz, R. M. Melnychuk, M. S. Stefanski, S. M. Copley, and T. Applied, Dynamic absorption of a powder layer, *Distribution* **1404**, 2 (2004).
- [16] A. Rubenchik, S. Wu, S. Mitchell, I. Golosker, M. LeBlanc, and N. Peterson, Direct measurements of temperature-dependent laser absorptivity of metal powders, *Appl. Opt.* **54**, 7230 (2015).
- [17] J. Trapp, A. M. Rubenchik, G. Guss, and M. J. Matthews, In situ absorptivity measurements of metallic powders during laser powder-bed fusion additive manufacturing, *Appl. Mater. Today* **9**, 341 (2017).
- [18] N. K. Tolochko, Y. V. Khlopkov, S. E. Mozzharov, M. B. Ignatiev, T. Laoui, and V. I. Titov, Absorptance of powder materials suitable for laser sintering, *Rapid Prototyp. J.* **6**, 155 (2000).
- [19] M. Rombouts, L. Froyen, A. V. Gusarov, E. H. Bentefour, and C. Glorieux, Light extinction in metallic powder beds: Correlation with powder structure, *J. Appl. Phys.* **98**, 1 (2005).
- [20] R. W. Mcvey and R. M. Melnychuk, Absorption of laser irradiation in a porous powder layer, **19** (2007).
- [21] M. Matthews, J. Trapp, G. Guss, and A. Rubenchik, Direct measurements of laser absorptivity during metal melt pool formation associated with powder bed fusion additive manufacturing processes, *J. Laser Appl.* **30**, 032302 (2018).
- [22] J. Ye, S. A. Khairallah, A. M. Rubenchik, M. F. Crumb, G. Guss, J. Belak, and M. J. Matthews, Energy coupling mechanisms and scaling behavior associated with laser powder bed fusion additive manufacturing, *Adv. Eng. Mater.* **21**, 1900185 (2019).
- [23] B. J. Simonds, J. Sowards, J. Hadler, E. Pfeif, B. Wilthan, J. Tanner, P. Williams, and J. Lehman, Time-Resolved Absorptance and Melt Pool Dynamics During Intense Laser Irradiation of Metal, *Phys. Rev. Appl.* **10**, 044061 (2018).
- [24] S. Ly, A. M. Rubenchik, S. A. Khairallah, G. Guss, and M. J. Matthews, Metal vapor micro-jet controls material redistribution in laser powder bed fusion additive manufacturing, *Sci. Rep.* **7**, 4085 (2017).
- [25] B. M. Lane, S. P. Moylan, E. P. Whinton, and L. Ma, in *Proc. Solid Free. Fabr. Symp.* (Austin, TX, 2015), pp. 575–591.
- [26] A. V. Gusarov, E. H. Bentefour, M. Rombouts, L. Froyen, C. Glorieux, and J. P. Kruth, Normal-directional and normal-hemispherical reflectances of micron- and submicron-sized powder beds at 633 and 790 nm, *J. Appl. Phys.* **99**, 113528 (2006).
- [27] Certain commercial equipment, software, and/or materials are identified in this paper in order to adequately specify the experimental procedure. In no case does such identification imply recommendation or endorsement by the National Institute of Standards. (n.d.).
- [28] E. J. Garboczi, Three-dimensional mathematical analysis of particle shape using X-ray tomography and spherical harmonics: Application to aggregates used in concrete, *Cem. Concr. Res.* **32**, 1621 (2002).
- [29] J. A. Slotwinski, E. J. Garboczi, P. E. Stutzman, C. F. Ferraris, S. S. Watson, and M. A. Peltz, Characterization of metal powders used for additive manufacturing, *J. Res. Natl. Inst. Stand. Technol.* **119**, 460 (2014).
- [30] E. J. Garboczi and J. W. Bullard, 3D analytical mathematical models of random star-shape particles via a combination of X-ray computed microtomography and spherical harmonic analysis, *Adv. Powder Technol.* **28**, 325 (2017).
- [31] N. Hrabec and E. J. Garboczi, Particle shape and size analysis for metal powders used for additive manufacturing: Techniques and application to two Ti64 powders, *Prep.* (2019).
- [32] J. C. Russ and F. B. Neal, *The Image Processing Handbook* (CRC Press, Boca Raton, FL, USA, 2016), 7th ed.
- [33] J. W. Carson and B. H. Pittenger, Bulk Properties of Powders, *ASM Handbook*, Vol. 7 Powder Met. Technol. Appl. **7**, 287 (1998).
- [34] J. E. Peterson and W. M. Small, Evaluation of metal powders using arnold density meter and hall flowmeter, *Powder Metall.* **37**, 37 (1994).

- [35] G. Jacob, A. Donmez, J. Slotwinski, and S. Moylan, Measurement of powder bed density in powder bed fusion additive manufacturing processes, *Meas. Sci. Technol.* **27**, 115601 (2016).
- [36] J. J. Valencia, Thermophysical Properties Sources and Availability of Reliable Data, ASM Handbook, Vol. 15 Cast. **15**, 468 (2008).
- [37] See the Supplemental material at <http://link.aps.org/supplemental/10.1103/PhysRevApplied.13.024057> for the individual 2D images used to make the 3D rendering of the powder found in Figure 3.
- [38] M. Suzuki, T. Shinmura, K. Limura, and M. Hirota, Study of the wall effect on particle packing structure using X-ray micro computed tomography, *Adv. Powder Technol.* **19**, 183 (2008).
- [39] J. M. R. Fernlund, The effect of particle form on sieve analysis: A test by image analysis, *Eng. Geol.* **50**, 111 (1998).
- [40] E. J. Garboczi, K. A. Riding, and M. Mirzahassemi, Particle shape effects on particle size measurement for crushed waste glass, *Adv. Powder Technol.* **28**, 648 (2017).
- [41] N. K. Tolochko, M. K. Arshinov, A. V. Gusarov, V. I. Titov, T. Laoui, and L. Froyen, Mechanisms of selective laser sintering and heat transfer in Ti powder, *Rapid Prototyp. J.* **9**, 314 (2003).
- [42] N. Martys and E. J. Garboczi, Length scales relating fluid permeability and electrical conductivity in model 2-D porous media, *Phys. Rev. B* **46**, 6080 (1992).
- [43] E. J. Garboczi, D. P. Bentz, and N. S. Martys, in *Methods in the Physics of Porous Media*, edited by P. Wong (Academic Press, Inc., San Diego, 1999), pp. 1–41.
- [44] A. V. Gusarov, I. Yadroitsev, P. Bertrand, and I. Smurov, Model of radiation and heat transfer in laser-powder interaction zone at selective laser melting, *J. Heat Transfer* **131**, 072101 (2009).
- [45] M. J. Matthews, G. Guss, S. A. Khairallah, A. M. Rubenchik, P. J. Depond, and W. E. King, Denudation of metal powder layers in laser powder bed fusion processes, *Acta Mater.* **114**, 33 (2016).
- [46] P. Bidare, I. Bitharas, R. M. Ward, M. M. Attallah, and A. J. Moore, Fluid and particle dynamics in laser powder bed fusion, *Acta Mater.* **142**, 107 (2018).
- [47] B. J. Simonds, J. W. Sowards, and P. A. Williams, Laser-induced fluorescence applied to laser welding of austenitic stainless steel for dilute alloying element detection, *J. Phys. D: Appl. Phys.* **50**, 325602 (2017).
- [48] R. Fabbro, in *Handb. Laser Weld. Technol.*, edited by S. Katayama (Woodhead Publishing Ltd., Cambridge, 2013), pp. 47–72.
- [49] J. Greses, P. A. Hilton, C. Y. Barlow, and W. M. Steen, Plume attenuation under high power Nd:Yttrium-aluminum-garnet laser welding, *J. Laser Appl.* **16**, 9 (2004).
- [50] Y. Kawahito, N. Matsumoto, M. Mizutani, and S. Katayama, Characterisation of plasma induced during high power fibre laser welding of stainless steel, *Sci. Technol. Weld. Join.* **13**, 744 (2008).
- [51] P. Y. Shcheglov, A. V. Gumenyuk, I. B. Gornushkin, M. Rethmeier, and V. N. Petrovskiy, Vapor-plasma plume investigation during high-power fiber laser welding, *Laser Phys.* **23**, 016001 (2013).
- [52] A. R. Nassar, T. J. Spurgeon, and E. E. Reutzel, Sensing defects during directed-energy additive manufacturing of metal parts using optical emissions spectroscopy, *Solid Free. Fabr. Proc.* **278**, 278 (2014).
- [53] S. Liu, W. Liu, M. Harooni, J. Ma, and R. Kovacevic, Real-time monitoring of laser hot-wire cladding of inconel 625, *Opt. Laser Technol.* **62**, 124 (2014).
- [54] L. Song and J. Mazumder, Real time Cr measurement using optical emission spectroscopy during direct metal deposition process, *IEEE Sens.* **12**, 958 (2012).
- [55] K. Bartkowiak, Direct laser deposition process within spectrographic analysis in situ, *Phys. Procedia* **5**, 623 (2010).
- [56] B. J. Simonds, P. Williams, and J. Lehman, Time-resolved detection of vaporization during laser metal processing with laser-induced fluorescence, *Procedia CIRP* **74**, 628 (2018).
- [57] A. Kramida, Y. Ralchenko, J. Reader, and N. A. Team, NIST Atomic Spectra Database (version 5.4) (2016).
- [58] T. Scholz, K. Dickmann, and A. Ostendorf, Investigation of the formation of nanoparticles during laser remote welding, *Phys. Procedia* **41**, 90 (2013).
- [59] J. Zou, W. Yang, S. Wu, Y. He, and R. Xiao, Effect of plume on weld penetration during high-power fiber laser welding, *J. Laser Appl.* **28**, 022003 (2016).
- [60] Y. Kawahito, K. Kinoshita, N. Matsumoto, and S. Katayama, Visualization of refraction and attenuation of near-infrared laser beam due to laser-induced plume, *J. Laser Appl.* **21**, 96 (2009).
- [61] T. A. Palmer, Unpublished result (n.d.).
- [62] S. T. Erdoğan, E. J. Garboczi, and D. W. Fowler, Shape and size of microfine aggregates: X-ray microcomputed tomography vs. laser diffraction, *Powder Technol.* **177**, 53 (2007).